RSC Advances

PAPER

View Article Online
View Journal | View Issue

Cite this: *RSC Adv.*, 2020, **10**, 36478

Application of soot discharged from the combustion of marine gas oil as an anode material for lithium ion batteries†

Hyun-Min Baek,[a] Dae-Yeong Kim,*[b] Won-Ju Lee *[c] and Jun Kang *[c]

Received 21st August 2020
Accepted 25th September 2020

DOI: 10.1039/d0ra07195a

rsc.li/rsc-advances

Many studies have recently investigated the characteristics of combustion products emitted from ships and onshore plant facilities for use as energy sources. Most combustion products that have been reported until now are from heavy oils, however, no studies on those from light oils have been published. This study attempted to use the combustion products from the light oils from naval ships as anode materials for lithium ion batteries (LIBs). These products have a carbon black morphology and were transformed into highly crystalline carbon structures through a simple heat treatment. These new structured materials showed reversible capacities of 544, 538, 510, 485, 451 and 395 mA h g^{-1} at C-rates of 0.1, 0.2, 0.5, 1.0, 2.0 and 5.0C, respectively, and excellent rate performance. These findings were the result of a combination hierarchical pores ranging from the meso- to macroscale and the high capacitive charge storage behavior of the soot. The results of this study prove that annealed soot with a unique multilayer graphite structure shows promising electrochemical performance suitable for the production of low-cost, high-performance LIB anode materials.

Introduction

Among the ~800 active naval ships worldwide (above 1000 t), those that do not use nuclear power (nuclear carrier, nuclear submarine) use marine gas oil (MGO), which is a light oil, as fuel. MGO is a very rational choice as the fuel for naval ships because it is mainly used in four-stroke medium- to high-speed diesel engines, it avoids the need for supplementary preheating devices, and it is easier to manage than gas fuels. The relatively high price of MGO is acceptable because naval ships are unique in that their economic efficiency is not considered.

The exhaust emissions from naval ships are not regulated by the International Maritime Organization (IMO). However, the United States Environmental Protection Agency (US EPA) and the Naval Sea Systems Command (NAVSEA) are now working together to classify the amounts of exhaust emissions of the military sector in accordance with the Intergovernmental Panel on Climate Change (IPCC)'s guidelines.[1] In addition, many member countries of the United Nations Climate Change Convention are calculating and reporting the emissions of their military sectors. Thus, efforts to manage exhaust emissions from naval ships are spreading worldwide.

The South Korean Navy is not yet regulating or controlling greenhouse gases (GHGs, *e.g.*, CO_2, CH_4, and N_2O) or particulate matters from naval ships, including soot emitted, and its ships use an annual total of approximately 124 000 t of MGO. When the GHGs are calculated using a method based on fuel quantity and caloric value, the estimated annual amount of emissions is approximately 395 000 CO_2-ton eq. Furthermore, when the soot emissions are calculated using the emission factor according to the operation patterns of the gas turbine, propulsion diesel engine, and power generation diesel engine, the total annual emission of soot is estimated to be 170 to 190 t.[2] Most of the soot emitted from naval ships is emitted together with the exhaust, whereas the soot accumulated in exhaust pipes is discharged after cleaning during the periodic repair of the engine. This soot must be incinerated during the process of being discarded, which causes an additional adverse effect on the atmospheric environment by further emitting greenhouse gases and particulate matters.

As a byproduct of the engine fuel for ships, soot accounts for 1–2% of the global emissions.[3] Among this soot, that emitted from the compression ignition engines of general ships using bunker oil or MDO has been researched for its application in electrode materials, such as the active and conductive materials for lithium ion batteries (LIBs), and its applicability after heat treatment has been sufficiently proven.[4,5] However, the soot emitted from naval ship engines or diesel engines using MGO has not yet been analyzed. To

[a]*2nd fleet, ROK Navy, Pyungtaek 17952, South Korea*

[b]*Department of Mechanical Engineering, Tokyo Institute of Technology, Meguro-ku, Tokyo 152-8550, Japan. E-mail: kim.d.as@m.titech.ac.jp*

[c]*Division of Marine Engineering, Korea Maritime and Ocean University, 727 Taejong-ro, Yeongdo-gu, Busan, 49112, Republic of Korea. E-mail: junkang@kmou.ac.kr; skywonju@kmou.ac.kr*

† Electronic supplementary information (ESI) available. See DOI: 10.1039/d0ra07195a

address this gap, this study characterizes the soot generated from naval ship diesel engines that only use MGO and examines its applicability as the active material for LIB anodes. Furthermore, previous studies required graphitization at 2000 °C or higher temperatures to manifest excellent performance as an electrode material for LIBs,[6] but this study found that a much lower temperature of 1000 °C was adequate. The results thus demonstrate the future potential of LIBs based on heat-treated soot collected from propulsion diesel engines for the guided missile frigate (FFG), the main battleship of the South Korean Navy (Fig. 1).

Materials and methods

Material preparation

This study used soot sampled from diesel engine exhaust pipes from an FFG operated by the South Korean Navy and its diesel engine as the target ship and engine. The FFG is a battleship with a full load of 3300 t, a light draft of 2300 t, a maximum speed of 30 kn, and a cruising speed of 18 kn. An analysis of the actual annual operation velocity patterns showed that its operation speed was around 8–12 kn for more than 80% of its total operation time. The target ship uses 100% MGO. Table S1† shows the specifications of the actually used MGO, and Table S2† shows the specifications of the target engine from which the sample was collected. The soot was sampled by opening the engine exhaust pipe, as shown in photographically in Fig. S1.†

Heat treatment

The collected soot was heat-treated to improve its crystallinity and to remove impurities such as oxygen and hydrogen. The soot was heated to 1000 °C at 25 °C min^{-1} in a tube furnace under flowing Ar. After a 60 minutes dwell time, it was cooled to room temperature at 7 °C min^{-1}.

Material characterization

An elemental analysis (EA) was performed before and after annealing using a Thermo Fisher Scientific EA1112. X-Ray diffraction (XRD) patterns were recorded on a Rigaku SmartLab X-ray diffractometer equipped with Cu Kα radiation ($\lambda = 1.5418$ Å). Raman spectra were obtained using a Lambda Ray P-1 Raman spectrometer with 532 nm laser excitation. Transmission electron microscopy (TEM) images were acquired on a JEOL 2010 at an acceleration voltage of 200 kV. Nitrogen sorption isotherms were measured on a MicrotracBEL Corp Belsorp-max. All samples were degassed at 200 °C for 3 h prior to the measurement. The specific surface area was calculated by the Brunauer–Emmett–Teller (BET) method. X-ray photoelectron spectroscopy (XPS) was performed using mono Al Kα radiation with a Thermo Fisher Scientific ESCALAB 250 spectrometer.

Electrochemical testing

Typically, a slurry of 70 wt% active material, 20 wt% carbon black, and 10 wt% polyacrylic acid (PAA) in distilled water was coated onto a copper foil current collector (~2.4 mg of active material on each electrode) and then dried at 80 °C overnight in a vacuum oven. The obtained electrode, a polypropylene separator, and a Li metal counter electrode were assembled into a 2032-type coin cell filled with an electrolyte in an Ar-filled glovebox. The electrolyte was 1 M $LiPF_6$ in ethylene carbonate (EC) and dimethyl carbonate (DEC) (1 : 1). Cyclic voltammetry (CV) was performed in the voltage range of 0.01–3.0 V (*vs.* Li^+/Li) using the BCS-805 Biologic battery test system, which was also used to carry out galvanostatic charge/discharge tests. Using this same system, electrochemical impedance spectroscopy (EIS) was conducted with a sine wave with a 5 mV perturbation amplitude over a frequency range of 10 kHz to 0.01 Hz.

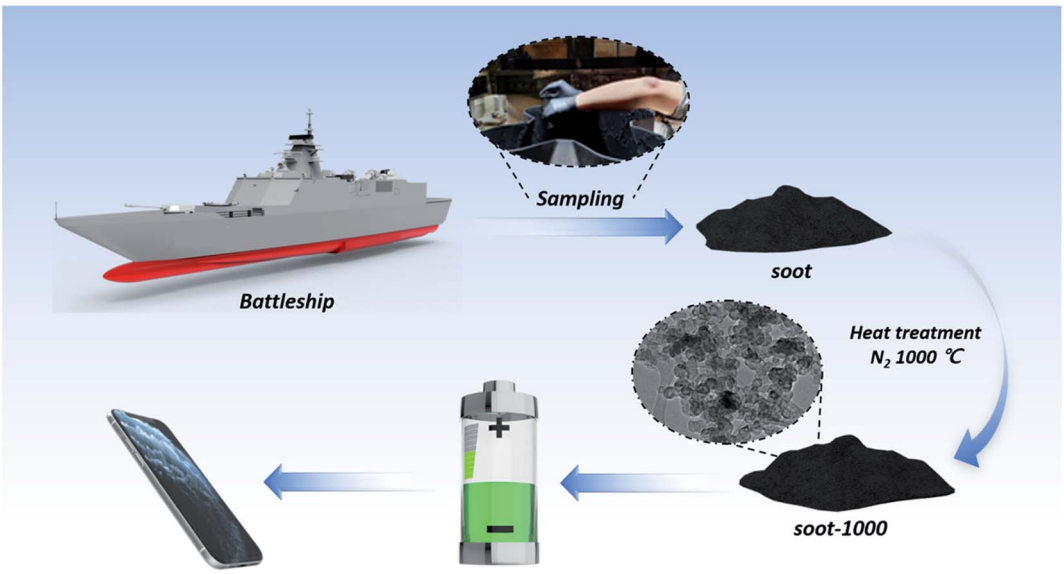

Fig. 1 Schematic diagram of fabrication of the soot-1000 and application for LIBs.

Table 1 EA results of soot and soot-1000: atomic percentages of C, H, N, S and O, respectively

	Element				
Sample	C	H	N	S	O
Soot	84.42	0.19	1.06	2.2	12.13
Soot-1000	96.8	—	1.06	2.14	—

Results and discussion

The chemical composition of the sampled soot is highly dependent on the fuel source and annealing process. The detailed chemical composition of soot used in this study was analyzed by EA before and after annealing (soot and soot-1000, respectively), as outlined in Table 1. Soot-1000 has a higher C content than soot, and O and H are not observed. However, in both samples, the N and S contents appear to be negligible (lower than 2.2 at%). The graphitization effect according to the annealing process was first verified by XRD patterns. In relation to the (002) and (100) planes of graphite, the results demonstrate that the amorphous structure of the soot before annealing became more crystalline, as shown in Fig. 2a. Two diffraction peaks appear near 25° and 44°, which become more narrow after annealing. Among these peaks, the (002) diffraction peak is related to the parallel lamination of graphene sheets, and the (100) peak corresponds to the honeycomb structure composed of sp^2 hybridized carbon.[7] From the (002) diffraction peak, the d_{002} spacing values for the soot and soot-1000 are calculated using Bragg's formula to be 0.35 nm and 0.36 nm, respectively, which are both larger than that of conventional graphite (0.3354 nm). A larger d_{002} spacing is more advantageous for Li^+ insertion and extraction and thus can increase the Li^+ storage capacity.[8] The Raman spectra (Fig. S2†) of soot and soot-1000 show a D-band at ~1340 cm^{-1} and a G-band at ~1560 cm^{-1}. The former is caused by the A_{1g} vibration of carbon aromatic rings caused by defects, and the latter corresponds to the E_{2g} vibration of sp^2 carbon.[9] Therefore, the appearance of the D-band can essentially be attributed to the amorphous structure of the soot. The intensity ratio of D-band and G-band I_D/I_G is widely used to determine the degree of disordering in carbon materials,[9–11] and in the case of soot, I_D/I_G decreased from 0.83 to 0.80 depending, on the annealing process. Meanwhile, the annealing process at 1000 °C evidently improves the electrical conductivity by removing O and H from the soot. In addition, annealing caused graphitization or graphenization in small domains, as evidenced by the formation of a sequence of *a–b* planes, which was subsequently analyzed in more depth through XPS. Fig. 2b illustrates the XPS survey spectra of soot and soot-1000. Both samples showed strong C 1s and O 1s peaks, as well as negligible N 1s and S 2p peaks, but no other elements were observed. In the soot, the atomic percentages of C, O, N, and S were 87.22, 11.72, 0.83 and 0.23 at%, respectively. In soot-1000, they were 96.68, 0.58, 2.34 and 0.4 at%, respectively. The trend in the elemental composition before and after annealing according to XPS was consistent with the EA results. The high-resolution C 1s spectra of the two samples (Fig. 2c) can be separated into four different peaks caused by sp^2 C–C (284.8 eV), C–OH (285.5 eV), O=C–O (288.5 eV), and π–π* shakeup (290.5 eV).[12–14] The area percentages of each peak are listed in Table 2. Evidently, the annealing process significantly decreased the peaks caused by O binding and increased the sp^2 C–C peak area. These changes imply that graphitization was partially increased by the annealing process, which supports the XRD results.

Fig. 3a shows the TEM images of soot-1000, which was found to be similar to carbon black, with a network of particles having primary particle sizes of approximately 30–40 nm (the TEM image of soot is shown in Fig. S3a†). A spherical morphology is often advantageous for electrode materials because it enables a uniform current distribution, which can decrease the electrolyte decomposition and prevent the formation of dendrites, ultimately improving the safety of LIBs. Moreover, the nanoparticles provide fast mass transport and minimize polarization effects by effectively shortening the diffusion length of Li.[15]

Table 2 XPS peak area percentages for different carbon configurations in soot and soot-1000

	Bonding			
Sample	sp^2 C–C (area%)	C–OH (area%)	O=C–O (area%)	π–π* shakeup (area%)
Soot	65.2	25.6	6.5	2.7
Soot-1000	75.5	15.9	3.6	5.0

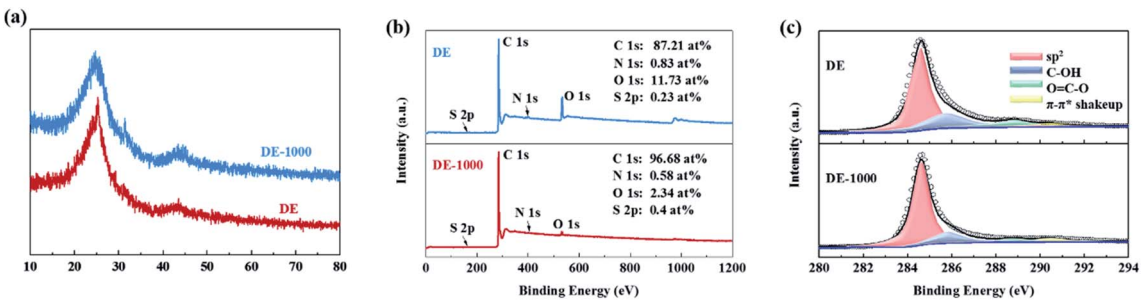

Fig. 2 (a) XRD patterns, (b) survey XPS spectrum, and (c) C 1s high-resolution XPS spectra of soot and soot-1000.

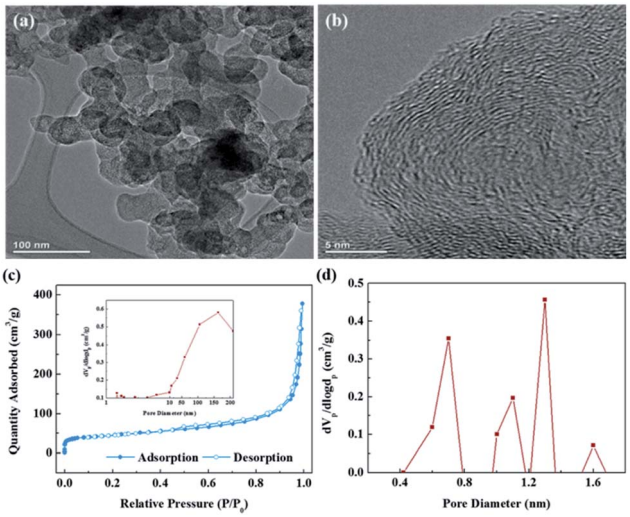

Fig. 3 (a) TEM and (b) HR-TEM images of soot-1000, (c) nitrogen sorption isotherm of soot-1000 (inset: BJH pore size distribution), and (d) micropore size distribution, calculated from adsorption isotherms using the MP method.

Meanwhile, no distinct changes were observed in the morphology or size distribution after annealing. Fig. 3b shows the high-resolution TEM (HR-TEM) image of soot-1000, and Fig. S3b† shows the corresponding image of the soot. Both soot and soot-1000 contain layers of graphene with distinct curves longer than 3 nm, and these layers are often stacked in turbostratic nanodomains. This turbostratic structure can experience lithiation at a slightly higher potential and can accept more Li^+ in the micropores and disorderly middle layer.[16]

The pore characteristics of soot and soot-1000 was verified by N_2 sorption analysis, and the results are shown in Fig. S4† and 3c, d. The BET surface areas of the two samples are 114.55 $m^2\ g^{-1}$ and 157.83 $m^2\ g^{-1}$, respectively. The pore size distribution curves of both soot and soot-1000 were calculated using the Barrett–Joyner–Halenda (BJH) method (insets, Fig. S2a† and 3c), which show a broad range of hierarchical pores from the meso- to the macroscale. Furthermore, the corresponding adsorption/desorption plots show type-II isotherms having a H3-type hysteresis loop. Meanwhile, Fig. S4b† and 3d show the distribution of micropores in the soot before and after annealing plotted using the micropore analysis (MP) method, which confirmed the existence of micropores and cavities according to the defect sites of the two samples. According to a previous study, Li can deposit in micropores and cavities in the size range of 0.5 to 1.5 nm, which can contribute to a high reversible capacity.[17] Soot-1000 exhibited a higher distribution of micropores than the soot, similar to the tendency of the specific surface area demonstrated by the BET analysis.

Moreover, soot-1000 also showed a higher volume of micropores (0.04 and 0.051 $cm^3\ g^{-1}$ for soot and soot-1000, respectively). This difference suggests that annealing partially activates the soot and increases its specific surface area and porosity. A high specific surface area can provide a sufficient electrode/electrolyte interface for the accumulation of ions or charges. Hierarchical pores with diameters ranging from the meso- to the macroscale are more advantageous for the rapid diffusion of ions and can provide a much higher rate performance.[18,19]

The electrochemical performance of soot-1000 as an anode material for LIBs is presented in Fig. 4. Fig. 4a shows the charge/discharge profiles of soot-1000 during the initial three cycles at a C-rate of 0.2C (1.0C = 372 mA h g^{-1}) in the voltage range of 0.01–3.0 V. The initial reversible capacity of soot-1000 was 429 mA h g^{-1}, which is slightly higher than the theoretical capacity for graphite (372 mA h g^{-1}). The sloping profile and initial reversible capacity imply that the lithium storage mechanism of soot-1000 is different from that of graphite. Specifically,

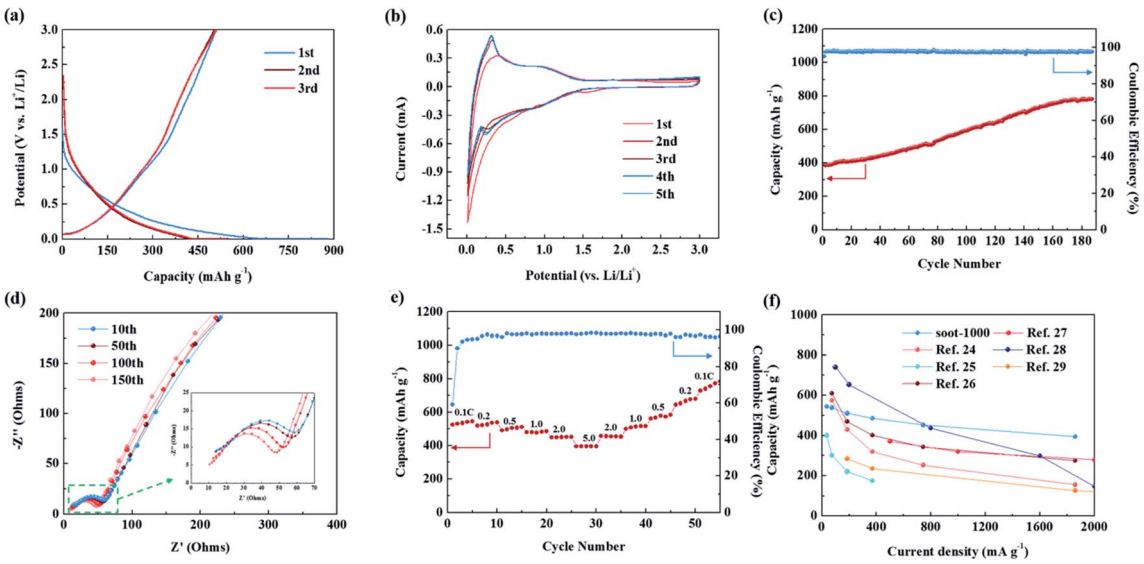

Fig. 4 Electrochemical performance of soot-1000 for LIB anodes: (a) charge/discharge profiles of the initial three cycles at 0.2C (1C = 372 mA h g^{-1}), (b) CV curves of the initial five cycles at a scan rate of 0.2 mV s^{-1}, (c) cycling performance at 1C, (d) EIS after different cycles. (e) Rate performance at different C-rates. (f) comparison of soot-1000 with representative recyling carbonaceous materials.

a sloping profile with no distinct plateau region suggests the capacitive charge storage behavior of soot-1000. Meanwhile, lithiation at a higher potential with a sloping profile can generate a safer anode material than commercial graphite, which has a dendrite growth problem owing to the Li interactions at a low potential. The initial coulombic efficiency of soot-1000 was approximately 57% at 0.2C. The initial capacity loss is caused by irreversible lithium ion trapping in the disorderly structure of carbon as well as the large specific surface area (157.83 $m^2\ g^{-1}$) enabling the formation of solid electrolyte interface (SEI) films that, which is consistent with the BET results. Continuously trapped lithium ions can be fractured during the initial capacity fading period and can re-form a thick SEI layer. Fig. 4b shows the CV curves of the first five cycles of soot-1000 at the scan rate of 0.2 mV s^{-1}. The irreversible integral area of the first and second cycles is caused by the irreversible storage of Li^+ in the disorderly structure, the formation of SEI films, and electrolyte decomposition.[20] These phenomena are consistent with the charge/discharge profile analysis. The cathodic peak at 0.01–0.2 V is due to the reversible Li^+ insertion in the graphite layer, and the anodic peak near 0.25 V is caused by Li extraction from the graphite layer. In the third cycle, a peak is observed near 0.25 V, which is considered to be caused by the efficient re-activation of the nanostructure of the hierarchical pores. During subsequent cycling, the CV curves overlap, which indicates the excellent reversibility of soot-1000 electrode.

Fig. 4c illustrates the cycling performance of soot-1000 at 1.0C. Similar to most carbon-based materials for LIBs, the coulombic efficiency was degraded by the formation of SEI films during the initial cycles. However, during subsequent cycling, the coulombic efficiency significantly improved, remarkably converging to 100%. Owing to gradual activation during the cycling process, the reversible capacity more than doubled after 181 cycles from 389 to 781 mA h g^{-1}. This phenomenon is typical for porous carbon materials and verifies the effect of the hierarchically porous structure of soot-1000.[18,21,22]

This was confirmed by EIS measurements after different numbers of cycles. In the medium- and high-frequency regions of the Nyquist plots in Fig. 4d, the semicircles and sloping straight lines appear after all numbers of cycles, which are affected by the charge-transfer resistance and solid-state diffusion of lithium in the electrode material, respectively.[13,23] The obvious changes in the semicircle in the medium-to-high-frequency region suggest that the charge-transfer resistance decreases with the increasing number of cycles. This reveals the excellent conductivity of the material at the interface between the electrolyte and the electrode material, as well as the activation of the electrode material, facile electrolyte penetration, and high lithium ion transfer rate.[22]

Soot-1000 also shows notable rate performance (Fig. 4e), which is critical to actual LIB applications. Specifically, at 0.1, 0.2, 0.5, 1.0, 2.0 and 5.0C, the reversible capacity values were 544, 538, 510, 485, 451 and 395 mA h g^{-1}, respectively, showing excellent rate performance. Moreover, when the current was restored to the initial 0.1C, the reversible capacity shows a higher value of 783 mA h g^{-1} than the initial value at 0.1C owing to the gradual activation (charge/discharge profiles are depicted in Fig. S5†). The electrochemical performance of soot-1000 is superior or similar to that of previously reported carbon materials derived from carbon sources such as rice hulls, wheat flour, and cork stalk cores, as summarized in Table S3† and Fig. 4f.[24–29]

Meanwhile, to further understand the rate performance of our LIBs, we analyzed the reaction kinetics *via* CV, and the results are shown in Fig. 5. The CV curves in the scan rate range of 0.2 to 1.0 mV s^{-1} (Fig. 5a) are almost identical, which suggests capacitive charge storage behavior. According to previous studies, the capacitive charge storage behavior can be verified using the following equation:[30]

$$I = av^b$$

where the b value is determined from the slope of log I *vs.* log v curves. The b values of the cathodic and anodic peaks are 0.6886 and 0.7336, respectively (Fig. 5b). A b value close to 0.5 means a diffusion-controlled process, whereas a b value approaching 1.0 means more surface-capacitive behavior. The ratio of capacitive charge storage behaviors can be quantified according to the research of Dunn.[31,32] At a fixed potential, the relative contributions of the diffusion-controlled process and the capacitive charge storage process can be derived from the following equation:

$$i(V) = k_1 v + k_2 v^{1/2}$$

As shown in Fig. 5c, the capacitive charge storage process at the scan rate of 1.0 mV s^{-1} is 82.1% of the total charge storage, and the contribution of the capacitive charge storage process gradually increases with the scan rate (Fig. 5d). Meanwhile, the capacitive charge storage behavior is mainly due to Li adsorbed onto the carbon surface. This storage mechanism has faster kinetics than insertion in the carbon lattice of Li to form LiC_6.

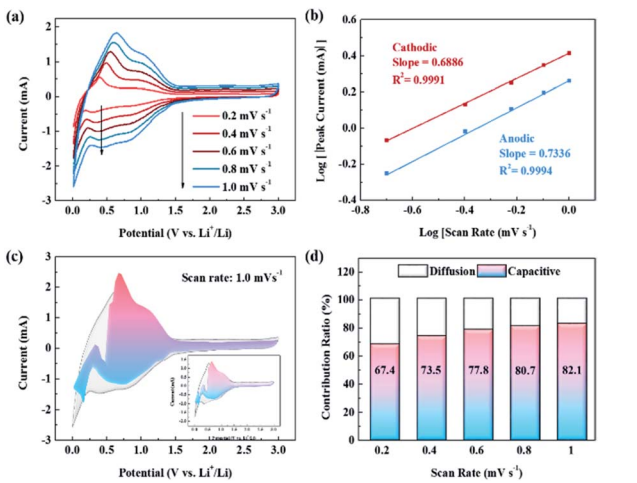

Fig. 5 (a) CV curves of soot-1000 at different scan rates from 0.2 to 1.0 mV s^{-1}, (b) linear relationship between the logarithms of the cathodic and anodic peak currents and the scan rate for soot-1000, (c) CV curve and capacitive contribution (blue shaded area) of soot-1000 at scan rates of 0.6 mV s^{-1} (inset) and 1.0 mV s^{-1}, and (d) corresponding capacitive contribution ratio to the total capacity at different scan rates.

Thus, the excellent rate performance of soot-1000 can be concluded to be due to a combination of hierarchical pores ranging from meso- to macropores and the highly capacitive charge storage behavior.

The above results show that soot-1000, which was derived from the diesel engine of a battleship, is an excellent electrode material for LIBs. Its excellent electrochemical performance can be explained by its novel nanostructure. First, soot-1000 is a turbostratic structure that can accommodate more Li^+ in the micropores and the disorderly middle layer, which can contribute to its high reversible capacity. Second, its nanostructure shortens the diffusion pathways. Third, hierarchical pores ranging from meso- to macropores can provide fast ion transport, which increases electrochemical activity by minimizing the diffusion resistance to mass transport at the large electrode/electrolyte interface. Moreover, these advantages combined with its highly capacitive storage behavior can contribute to its excellent rate performance.

Conclusions

This study represents the first attempt to recycle the combustion products from engines of naval ships using MGO into active materials for LIBs. This unique concept can transform waste into an energy source. A heat treatment at only 1000 °C increased the crystallinity of the collected soot, and the d_{002} spacing of the soot both before and after annealing was larger than that of graphite. The annealed soot was then used as an active material for LIB anodes. The attained morphology and structure of the soot were investigated using HR-TEM, and the soot was found to be similar to carbon black, with a network of particles having primary particle sizes of approximately 30–40 nm. The XRD, Raman spectroscopy, and BET surface area results showed that the graphitized soot was transformed to highly crystalline graphite, and the specific surface area of the graphitized soot was larger than that generally used in active materials (1–2 $m^2 g^{-1}$).

The annealed soot exhibited a unique multilayer graphite structure that facilitated its electrochemical performance, which makes it a suitable candidate for the anode active material. In addition, its rate performance was excellent, unlike that of similar combustion products that have been reported thus far. Currently, the types of fuel oils used in commercial ships as well as naval ships are changing. Therefore, the same analysis and research should be conducted for different types of soot emitted from these ships, and similar studies should be conducted to find various uses of waste soot.

Conflicts of interest

There are no conflicts to declare.

Notes and references

1 US EPA, *Inventory of US greenhouse gas emissions and sinks: 1990–2011*, United States Environmental Protection Agency, Washington DC, 2013, vol. 505.
2 C. Trozzi, *Emission estimate methodology for maritime navigation*, Techne Consulting, Rome, 2010.
3 D. Lack, B. Lerner, C. Granier, T. Baynard, E. Lovejoy, P. Massoli, A. Ravishankara and E. Williams, Light absorbing carbon emissions from commercial shipping, *Geophys. Res. Lett.*, 2008, **35**, L13815.
4 W.-J. Lee, H. V. Kim, J.-H. Choi, G. Panomsuwan, Y.-C. Lee, B.-S. Rho and J. Kang, Recycling waste soot from merchant ships to produce anode materials for rechargeable lithium-ion batteries, *Sci. Rep.*, 2018, **8**, 1–10.
5 J.-H. Choi, D.-Y. Kim, W.-J. Lee and J. Kang, Conversion of Black Carbon Emitted from Diesel-Powered Merchant Ships to Novel Conductive Carbon Black as Anodic Material for Lithium Ion Batteries, *Nanomaterials*, 2019, **9**, 1280.
6 W.-J. Lee, D.-Y. Kim, J.-H. Choi, J.-W. Lee, J.-S. Kim, K. Son, M.-J. Ha and J. Kang, Utilization of petroleum coke soot as energy storage material, *Energies*, 2019, **12**, 3195.
7 J. Yang, Z. Ju, Y. Jiang, Z. Xing, B. Xi, J. Feng and S. Xiong, Enhanced capacity and rate capability of nitrogen/oxygen dual-doped hard carbon in capacitive potassium-ion storage, *Adv. Mater.*, 2018, **30**, 1700104.
8 J. Ou, Y. Zhang, L. Chen, Q. Zhao, Y. Meng, Y. Guo and D. Xiao, Nitrogen-rich porous carbon derived from biomass as a high performance anode material for lithium ion batteries, *J. Mater. Chem. A*, 2015, **3**, 6534–6541.
9 A. C. Ferrari and D. M. Basko, Raman spectroscopy as a versatile tool for studying the properties of graphene, *Nat. Nanotechnol.*, 2013, **8**, 235–246.
10 F. Niu, J. Yang, N. Wang, D. Zhang, W. Fan, J. Yang and Y. Qian, $MoSe_2$-Covered N, P-Doped Carbon Nanosheets as a Long-Life and High-Rate Anode Material for Sodium-Ion Batteries, *Adv. Funct. Mater.*, 2017, **27**, 1700522.
11 G. Ma, K. Huang, J.-S. Ma, Z. Ju, Z. Xing and Q.-c. Zhuang, Phosphorus and oxygen dual-doped graphene as superior anode material for room-temperature potassium-ion batteries, *J. Mater. Chem. A*, 2017, **5**, 7854–7861.
12 S. Alvin, D. Yoon, C. Chandra, H. S. Cahyadi, J.-H. Park, W. Chang, K. Y. Chung and J. Kim, Revealing sodium ion storage mechanism in hard carbon, *Carbon*, 2019, **145**, 67–81.
13 X. Hu, X. Sun, S. J. Yoo, B. Evanko, F. Fan, S. Cai, C. Zheng, W. Hu and G. D. Stucky, Nitrogen-rich hierarchically porous carbon as a high-rate anode material with ultra-stable cyclability and high capacity for capacitive sodium-ion batteries, *Nano Energy*, 2019, **56**, 828–839.
14 G. Xia, C. Wang, P. Jiang, J. Lu, J. Diao and Q. Chen, Nitrogen/oxygen co-doped mesoporous carbon octahedrons for high-performance potassium-ion batteries, *J. Mater. Chem. A*, 2019, **7**, 12317–12324.
15 V. G. Pol and M. M. Thackeray, Spherical carbon particles and carbon nanotubes prepared by autogenic reactions: Evaluation as anodes in lithium electrochemical cells, *Energy Environ. Sci.*, 2011, **4**, 1904–1912.
16 V. Etacheri, C. Wang, M. J. O'Connell, C. K. Chan and V. G. Pol, Porous carbon sphere anodes for enhanced lithium-ion storage, *J. Mater. Chem. A*, 2015, **3**, 9861–9868.

17 P.-Y. Chang and R.-a. Doong, Microwave-assisted synthesis of SnO_2/mesoporous carbon core-satellite microspheres as anode material for high-rate lithium ion batteries, *J. Alloys Compd.*, 2019, **775**, 214–224.

18 J. Hou, C. Cao, F. Idrees and X. Ma, Hierarchical porous nitrogen-doped carbon nanosheets derived from silk for ultrahigh-capacity battery anodes and supercapacitors, *ACS Nano*, 2015, **9**, 2556–2564.

19 J. He, N. Wang, Z. Cui, H. Du, L. Fu, C. Huang, Z. Yang, X. Shen, Y. Yi and Z. Tu, Hydrogen substituted graphdiyne as carbon-rich flexible electrode for lithium and sodium ion batteries, *Nat. Commun.*, 2017, **8**, 1–11.

20 H. Tabassum, R. Zou, A. Mahmood, Z. Liang, Q. Wang, H. Zhang, S. Gao, C. Qu, W. Guo and S. Guo, A universal strategy for hollow metal oxide nanoparticles encapsulated into B/N Co-doped graphitic nanotubes as high-performance lithium-ion battery anodes, *Adv. Mater.*, 2018, **30**, 1705441.

21 J. Tang, G. Chen, J. Yang, X. Zhou, L. Zhou and B. Huang, Silica-assistant synthesis of three-dimensional graphene architecture and its application as anode material for lithium ion batteries, *Nano Energy*, 2014, **8**, 62–70.

22 L. Wang, B. Lu, S. Wang, W. Cheng, Y. Zhao, J. Zhang and X. Sun, Ultra-high performance of Li/Na ion batteries using N/O dual dopant porous hollow carbon nanocapsules as an anode, *J. Mater. Chem. A*, 2019, **7**, 11117–11126.

23 H. Hou, L. Shao, Y. Zhang, G. Zou, J. Chen and X. Ji, Large-area carbon nanosheets doped with phosphorus: a high-performance anode material for sodium-ion batteries, *Adv. Sci.*, 2017, **4**, 1600243.

24 K. Yu, Y. Wang, X. Wang, W. Liu, J. Liang and C. Liang, Preparation of porous carbon anode materials for lithium-ion battery from rice husk, *Mater. Lett.*, 2019, **253**, 405–408.

25 D. G. Lim, K. Kim, M. Razdan, R. Diaz, S. Osswald and V. G. Pol, Lithium storage in structurally tunable carbon anode derived from sustainable source, *Carbon*, 2017, **121**, 134–142.

26 Y. Li, C. Li, H. Qi, K. Yu and C. Liang, Mesoporous activated carbon from corn stalk core for lithium ion batteries, *Chem. Phys.*, 2018, **506**, 10–16.

27 V. Selvamani, R. Ravikumar, V. Suryanarayanan, D. Velayutham and S. Gopukumar, Garlic peel derived high capacity hierarchical N-doped porous carbon anode for sodium/lithium ion cell, *Electrochim. Acta*, 2016, **190**, 337–345.

28 I. Elizabeth, B. P. Singh, S. Trikha and S. Gopukumar, Bio-derived hierarchically macro-meso-micro porous carbon anode for lithium/sodium ion batteries, *J. Power Sources*, 2016, **329**, 412–421.

29 P. Zheng, T. Liu, J. Zhang, L. Zhang, Y. Liu, J. Huang and S. Guo, Sweet potato-derived carbon nanoparticles as anode for lithium ion battery, *RSC Adv.*, 2015, **5**, 40737–40741.

30 G. Zhao, D. Yu, H. Zhang, F. Sun, J. Li, L. Zhu, L. Sun, M. Yu, F. Besenbacher and Y. Sun, Sulphur-doped carbon nanosheets derived from biomass as high-performance anode materials for sodium-ion batteries, *Nano Energy*, 2020, **67**, 104219.

31 J. Wang, J. Polleux, J. Lim and B. Dunn, Pseudocapacitive contributions to electrochemical energy storage in TiO2 (anatase) nanoparticles, *J. Phys. Chem. C*, 2007, **111**, 14925–14931.

32 V. Augustyn, P. Simon and B. Dunn, Pseudocapacitive oxide materials for high-rate electrochemical energy storage, *Energy Environ. Sci.*, 2014, **7**, 1597–1614.

